
NeRF-SUPERVISED FEATURE POINT DETECTION AND DESCRIPTION

Ali Youssef

Department of Computer Science
University College London
ali.youssef.22@ucl.ac.uk

Francisco Vasconcelos*

Department of Computer Science
University College London
f.vasconcelos@ucl.ac.uk

ABSTRACT

Feature point detection and description is the backbone for various computer vision applications, such as Structure-from-Motion, visual SLAM, and visual place recognition. While learning-based methods have surpassed traditional handcrafted techniques, their training often relies on simplistic homography-based simulations of multi-view perspectives, limiting model generalisability. This paper introduces a novel approach leveraging neural radiance fields (NeRFs) for realistic multi-view training data generation. We create a diverse multi-view dataset using NeRFs, consisting of indoor and outdoor scenes. Our proposed methodology adapts state-of-the-art feature detectors and descriptors to train on NeRF-synthesised views supervised by perspective projective geometry. Our experiments demonstrate that the proposed methods achieve competitive or superior performance on standard benchmarks for relative pose estimation, point cloud registration, and homography estimation while requiring significantly less training data compared to existing approaches.

Keywords Feature detection and description · Neural Radiance Fields · Datasets

1 Introduction

Feature point detection and description under different scene viewpoints is a common starting point for many multi-view problems including Structure-from-Motion [1], visual SLAM [2, 3], or visual place recognition [4, 5]. In the past decade, different learning-based approaches to this problem [6, 7, 8, 9] have replaced handcrafted techniques in many applications [10, 11, 12]. Crucially, most of these models can be fine-tuned in a self-supervised manner on any single-view dataset. This is achieved by applying different homography warpings to the training data, simulating different viewpoints of the same scene with known point-to-point "ground-truth" mappings. While this training scheme is simple and flexible, the generated homography warpings are a crude simplification of multi-view perspective, which can lead to limited model generalisability.

This paper aims at leveraging image synthesis with neural radiance fields (NeRFs) as a more realistic way of generating multi-view training data for feature detection and description models (see Fig. 1). Since NeRFs require multi-view data to synthesise novel views, we can no longer rely on the single image datasets typically used for training the above mentioned homography-based methods. We therefore create our own dataset consisting of both indoor and outdoor image sequences around static scenes, and reconstruct all of them with NeRFacto [13]. This enables the generation of arbitrary viewpoints of each scene consistent with a pinhole projective model with known point-to-point mappings via point re-projection. We propose a general methodology to upgrade state-of-the-art homography-based methods to train them on projective views synthesised from NeRF-type algorithms. Our contributions are as follows:

- We create a new multi-view dataset consisting of images from 10 different indoor and outdoor scenes, and a total of 10000 NeRF-synthesised views from these scenes with corresponding depth maps, intrinsic and extrinsic parameters.

*Wellcome / EPSRC Centre for Interventional and Surgical Sciences (WEISS).



Figure 1: **Visual representation of multi-view data.** Learning-based detectors and descriptors achieve supervision on single-view datasets by simulating different viewpoints through homographic warpings to the input image I (see Fig. 1a) resulting in I' (see Fig. 1b). While we achieve supervision by directly sampling a NeRF rendered image from a different viewpoint (see Fig. 1c).

- We propose two general methodologies (end-to-end and projective adaptation) to train state-of-the-art point detection and description methods using a loss function based on NeRF re-projection error.
- We re-train adapted versions of SuperPoint [6] and SiLK [14] using our NeRF-synthesised data and compare them against the original baselines trained on the much larger MS-COCO dataset. We outperform the original baselines for relative pose estimation on ScanNet and YFCC100M datasets, similar performance for pairwise point cloud registration, while only slightly under-performing on the HPatches homography estimation benchmark.

2 Related Work

Research on multi-view feature detection and description has a large focus on creating representations invariant to geometric transformations (e. g. scale, rotation, affinity) and to illumination conditions, so that the same scene point can be reliably recognised and matched regardless of its viewpoint. Classic methods achieved this by handcrafting feature extractors that incorporate these invariance properties by design. Some of these decade-old methods stood the test of time and are still widely used today [15, 16]. More recently, the success of deep feature extraction enabled neural networks to learn these invariance properties from training data. Large open-source datasets [17, 18, 19] have been extensively employed to train either learning-based interest point detectors and descriptors [6, 20, 14, 21], or detector-free local feature matchers [22, 23, 24].

Some of these methods [6, 14] are trained in a self-supervised manner on uncalibrated RGB single-view datasets such as MS-COCO [17] by simulating multiple views as homography warpings. Other methods [20, 21] are trained with additional supervision using calibrated multi-view RGB-D datasets such as ScanNet [18]. These two classes of methods have pros and cons. The multi-view data generated by self-supervised methods is not representative of all possible viewpoint changes (homographies only model planar scenes or pure rotations) and thus it does not fully generalise to some application scenarios. On the positive side, they can be trained on arbitrarily large number of transformations and are also extremely flexible as they can be fine-tuned on any uncalibrated single-view dataset. Fully supervised methods are trained on more realistic multi-view data that covers full projective view changes with occlusions, however, the required training data is significantly more complex to obtain. The variety of scenes and viewpoint changes in the training data is also limited by the practicalities of real data acquisition. To get the best of both worlds, we propose using NeRF reconstructions obtained from RGB image sequences, which are both simple to acquire and enable the synthetic generation of arbitrary projective viewpoints beyond homographies.

Progress on image synthesis with NeRF and its variants [25, 26, 27] has exploded in the past years, with very fast improvements in computational efficiency, image synthesis quality, reconstruction accuracy, and input data requirements. As these techniques enable synthesising arbitrary viewpoints of a reconstructed scene, they can be used for rich data augmentation [28]. Most related to our work, they have been utilised to self-supervise multi-view methods for learning viewpoint invariant object descriptors [29], stereo disparity [30], and optical flow [31]. However, to the best of our knowledge NeRF self-supervision has been under-explored for point feature detection and description.

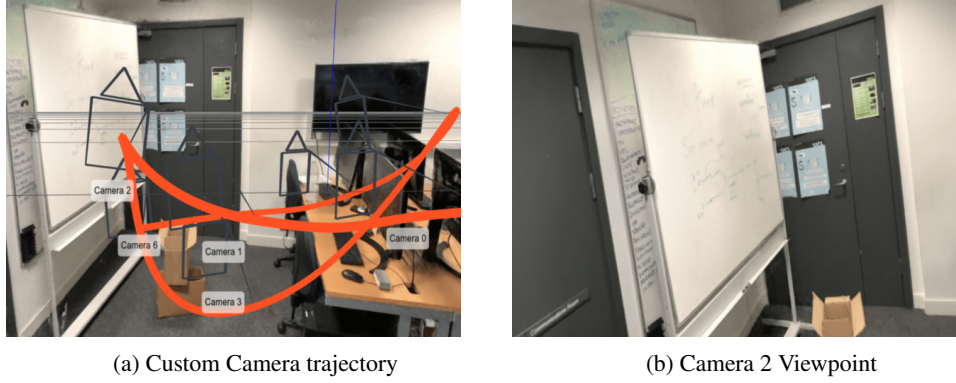


Figure 2: **Customised Camera Trajectory.** A visual representation of a custom camera trajectory in NeRF Studio’s [13] interactive real-time viewer. Fig. 2b demonstrates the viewpoint of Camera 2 in Fig. 2a.

3 Methodology

3.1 NeRF Dataset

We build a NeRF dataset for 10 indoor and outdoor scenes, containing in total 10000 synthetic images with their corresponding intrinsic/extrinsic parameters and depth maps. We note that this dataset is extremely small compared to what is typically used to train state-of-the-art feature detection (30 times smaller than MS-COCO, 250 times smaller than ScanNet). Our goal is to show that leveraging NeRF self-supervision enables state-of-the-art performance on multiple benchmarks with significantly less training data.

We captured four indoor and one outdoor scenes with an iPhone 10 at 4K resolution, one indoor and one outdoor scene with a Samsung A52 at 4k resolution. We also utilise two blender generated indoor scenes with images sourced from [32] and one outdoor scene publicly available through [33] as they are scenes that consist of high quality RGB images, while being are rich with features. While different training sets could be constructed using existing publicly available data, we focus on a trade-off between scene diversity and minimal dataset size.

We obtain camera poses for all images using COLMAP [34] and use them to generate synthetic views. We trained a Nerfacto model for each scene, which is part of the NeRFStudio framework [13] and merges improvements from a range of NeRF implementations [35, 33, 36, 37]. For each scene we rendered 1000 synthetic views and corresponding depth maps with 44° field of view and 640×480 resolution. We use NeRFStudio’s interactive real-time viewer to define custom camera trajectories for each scene that ensure diversity in viewpoints while maintaining global scene overlap. Trajectories consist of uniformly sampled smooth trajectories around the scene coupled with small rotations around the camera centre.

3.2 NeRF Point Re-Projection

Similarly to prior self-supervised methods [6, 14] we consider neural networks that, at inference time, detect interest point locations \mathbf{p} and extract their descriptors \mathbf{d} from a single view. Consider two views I, I' synthesised by NeRF with known intrinsic $(\mathcal{K}, \mathcal{K}')$ and extrinsic $(R, R', \mathbf{t}, \mathbf{t}')$ parameters. For any arbitrary point with homogeneous pixel coordinates \mathbf{p} in image I , we know its NeRF reconstructed depth d and can represent it in 3D world coordinates as:

$$\mathbf{P} = [R|\mathbf{t}] \frac{\mathbf{p}_c}{\|\mathbf{p}_c\|} d, \quad \mathbf{p}_c = \mathcal{K}^{-1}\mathbf{p}. \quad (1)$$

Similarly, \mathbf{P} can be re-projected into view I' as:

$$\mathbf{p} = \mathcal{K}' \frac{\mathbf{P}'}{\mathbf{P}'_z}, \quad \mathbf{P}' = [R'^T | -R'^T \mathbf{t}'] \mathbf{P}. \quad (2)$$

Assuming that reconstructed depths d are accurate, the above equations enable self-supervising a point detector, by designing a loss function that promotes a set of re-projected points \mathbf{p}' detected in view I to align with points independently detected on view I' . However, many distinctive interest points lie on scene edges at a depth discontinuity. In this case any small deviation in \mathbf{p} can result in large d variations corresponding to background and foreground depths.

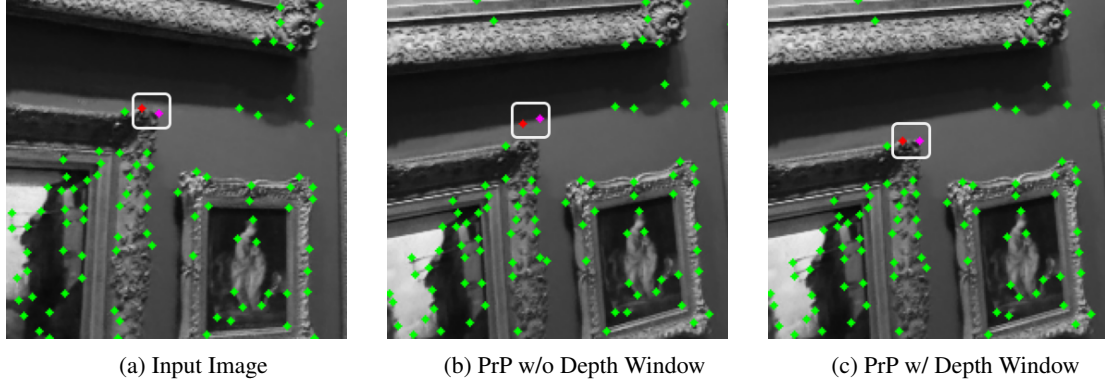


Figure 3: **Depth window estimation.** The interest points, depicted in red and purple situated at the painting’s frame in Fig. 3a, exhibit misprojection onto image I' without the depth window estimation method. However, misprojection errors are effectively mitigated by utilising the depth window estimation method as seen in Fig. 3c.

To make re-projection stable around edges, we focus on matching foreground objects only (minimising potential view occlusions). This can be achieved in a very simple manner by computing d as the minimum depth within a 5×5 pixel window centred in \mathbf{p} (see example in Fig. 3).

4 Implementations

4.1 SiLK-PrP

Self-supervised point detection methods that are trained end-to-end can be easily adapted to utilise NeRF training data. Using SiLK [14] as a baseline, we propose an adapted version that, during training, simply replaces homography warpings with NeRF renderings and point re-projection, while keeping the rest of the training pipeline and loss functions intact.

In the original SiLK approach, image pairs with ground-truth bi-directional correspondences are generated on-the-fly during training with homography warpings. We rely on our pre-rendered NeRF dataset described in section 3.1, to avoid significant computational overhead caused by on-the-fly image rendering. During training we randomly sample image pairs I, I' from the same scene, Eqs. 1 and 2 are then utilised during training to generate dense ground-truth point correspondences, discretised at pixel level.

4.2 SuperPoint-PrP

SuperPoint is a self-supervised method that goes through multiple stages of training. Firstly, an encoder with a detector head is trained in a fully supervised manner to detect corners on a synthetic dataset with simple geometric shapes. The pre-trained detector, called MagicPoint, is used to generate pseudo-ground truth interest points on a real dataset (*e.g.* MS-COCO) using a process called homographic adaptation. This involves generating several homography warped copies of a training image, passing them through the trained detector, unwarping all predictions back to the original training image, and finally aggregating all unwrapped predictions to generate the pseudo label. This process can be repeated several times, where after each round of homographic adaptation, the detector head is further trained, updating the pseudo-ground truth labels, while improving the detector head generalisability. After a final round of homographic adaptation, a descriptor head is added to the model, which is jointly trained with the whole model with an additional descriptor loss term on the real dataset resulting in the SuperPoint model.

With the NeRF training data approach, we use the same architecture of the original SuperPoint model. However, modify the homographic adaptation process as well as the descriptor loss to handle our NeRF training data and Point Re-Projection process.

4.2.1 Projective Adaptation

Similarly to our SiLK-PrP approach, we consider pre-rendered NeRF images as training data. In this case, we exploit the fact that training sequences for each scene are generated along a continuous trajectory.

We randomly sample from a window of 20 consecutive rendered NeRF images $I_{i \rightarrow i+19}$. We take pseudo ground-truth points for initial image I_i and random sample 15 of the remaining images as the warped versions of I_i .

The probability heatmap \mathbf{H}_i for image I_i is then computed, followed by randomly extracting 15 images out of the subsequent images. For each of the randomly selected image I_r , their probability heatmap \mathbf{H}_r is computed, and interest points \mathbf{p}_r are extracted from each heatmap, while using non-maximum suppression to filter out feature points that are too close to each other.

Once interest points \mathbf{p}_r are obtained, the PrP process is applied to project the interest points aligning them with the initial frame I_i , for clarity the projected interest points can be denoted as \mathbf{p}_i' .

Having obtained the projected interest points \mathbf{p}_i' , we generate a mask denoted as $\mathbf{B}_{i'}$, for each interest point in \mathbf{p}_i' coordinates on the binary mask, a 3x3 patch centred around the interest point before projection is extracted from the probability heatmap \mathbf{H}_r , the patch is then applied on the binary heatmap $\mathbf{B}_{i'}$. Thus, mask $\mathbf{B}_{i'}$, serves as the probability heatmap of rendered image I_r projected onto the input render frame I_i .

Finally, the input's rendered image probability heatmap \mathbf{H}_i and mask $\mathbf{B}_{i'}$ for each frame, are aggregated together, non-maximum suppression is applied once more to the final aggregated heatmap to obtain pseudo ground-truth interest points for the input rendered image I_i .

4.2.2 Descriptor Loss

SuperPoint's [6] loss consists of an interest point detection loss \mathcal{L}_p and the other for the descriptor \mathcal{L}_d .

The interest point detection loss is a cross entropy loss between the interest point detector prediction \mathcal{X} on the input image, and the ground truth interest points \mathcal{Y} . We effectively do not apply any modifications to the interest point detection loss.

SuperPoint's [6] descriptor loss \mathcal{L}_d , is a hinge loss between every pair of descriptors cells, $d_{h_w} \in \mathcal{D}$ from \mathcal{I} and $d_{h'w'} \in \mathcal{D}'$ from \mathcal{I}' . "Cells" are essentially pixels in lower dimension, where for an input image of size $H \times W$, a cell has a dimension of $H_c = \frac{H}{8} \times W_c = \frac{W}{8}$. In simpler terms, each pixel in the encoded image maps an 8×8 region of the input image. SuperPoint's descriptor loss can be defined as:

$$\mathcal{L}_d(D, D', S) = \frac{1}{(H_c W_c)^2} \sum_{h=1}^{H_c} \sum_{w=1}^{W_c} l_d(d_{h_w}, d'_{h'w'}; s_{hwh'w'}) \quad (3)$$

where S is a homography induced correspondence, defined as:

$$s_{hwh'w'} = \begin{cases} 1, & \text{if } \|\widehat{\mathcal{H}p_{h_w}} - p_{h'w'}\| \leq 8. \\ 0, & \text{otherwise} \end{cases} \quad (4)$$

where p_{h_w} is the centre pixel in the (h, w) cell, and $\widehat{\mathcal{H}p_{h_w}}$ is multiplying the centre pixel cell p_{h_w} by a homography \mathcal{H} which relates the input image and its warped pair.

We reformulate the homography induced correspondence of SuperPoint [6], in such a way that centre pixel p_{h_w} can be transformed using the PrP process rather than transforming it through homography \mathcal{H} . Let $\mathcal{C}(\cdot)$ represent a function that takes p_{h_w} as an input, along with all parameters utilised in the PrP process (see Eqs. 1 and 2), for simplicity, these parameters can be combined and denoted as M . Therefore, the PrP induced correspondence can be defined as:

$$s_{hwh'w'} = \begin{cases} 1, & \text{if } \|\mathcal{C}(M; p_{h_w}) - p_{h'w'}\| \leq 8. \\ 0, & \text{otherwise} \end{cases} \quad (5)$$

4.3 Implementation details

For all experiments, we present results using our own training pipeline for both SuperPoint-PrP and SiLK-PrP. Additionally, we report results for the baseline SuperPoint[6] model using our own reproduced implementation.

To mitigate misprojection errors during the PrP process, we employ a random sampling approach for selecting image I' from a subset of the training data. This subset is constrained within a range determined by a lower limit, λ_l , and an

upper limit, λ_u , based on the input image I . Specifically, we set λ_l to 70 and λ_u to 150, ensuring a balance between viewpoint changes while avoiding projection errors. Moreover, the depth rectification process threshold ϵ was set as $3e^{-2}$ meters.

Lastly, for SuperPoint-PrP and SiLK-PrP training, we apply the same photometric augmentation applied on the baseline models [6, 14] such as random brightness and contrast, Gaussian noise, motion blur, but do not apply homographic augmentation such as rotation, scaling or translation. Lastly, all models are trained using PyTorch [38] and a single NVIDIA RTX 3090 Ti GPU.

4.3.1 SiLK-PrP training.

SiLK-PrP is trained on the NeRF dataset in an end-to-end manner for a total of 100,000 iterations. We keep the same SiLK hyperparameters when training SiLK-PrP with ADAM optimiser, a learning rate of $1e^{-4}$ and betas as (0.9, 0.999), while the batch size was set as 1.

4.3.2 SuperPoint-PrP training.

Similar to SuperPoint’s baseline training pipeline, we obtain the base MagicPoint model by conducting training on the Synthetic Shapes dataset for 200,000 iterations. The MagicPoint model is identical to the SuperPoint model omitting the descriptor head, while the Synthetic Shapes dataset consists of synthetic 2D geometrical shapes such as lines, triangles and cubes.

To produce the MagicPoint-PrP model, we further train the base MagicPoint model through two rounds of Projective Adaptation on the NeRF dataset, each lasting 30,000 iterations. Finally, the SuperPoint-PrP model is obtained by training both the detector and descriptor heads of MagicPoint-PrP once again on the NeRF dataset for a total of 300,000 iterations. The training process is performed using the baseline SuperPoint model hyperparameters with ADAM optimiser, a learning rate of $1e^{-3}$ and betas set to (0.9, 0.999). The batch size is set at 32 for the MagicPoint-PrP model and 2 for the SuperPoint-PrP model.

5 Experiments

In this section, we assess the performance of the PrP-trained interest point detector and descriptor models in comparison to their corresponding baseline models. The evaluation encompasses accessing the interest point detection quality and homography estimation on the HPatches dataset [39]. Additionally, on ScanNet [18], we evaluate the indoor relative pose estimation and point cloud registration capabilities of each model. Lastly, we evaluate the outdoor relative pose estimation of each model using the YFCC100M [40] dataset. For all evaluations, we perform feature matching using mutual nearest neighbour. Through the aforementioned experiments, we analyse the following:

- Our NeRF dataset is approximately $\frac{1}{30}$ the size of the MS-COCO dataset [17], and $\frac{1}{250}$ the size of ScanNet’s [18]. Despite the relatively small scale of our training dataset, we analyse the generalisability of the NeRF-trained models on real-world data and numerous conditions across multiple datasets. Surprisingly, the PrP-models trained on our NeRF datasets consistently demonstrate comparable results in most evaluations. This poses the question of the necessity for large open-source datasets in training learning-based detectors and descriptors.
- Unlike [17, 18, 19, 41], our NeRF dataset fully consists of synthetic images of real scenes. Thus, we assess the interest point detection quality of the NeRF-trained detectors relative to their corresponding baseline models. Conducted experiments revealed that the quality of interest points generated by NeRF-trained models remained consistently high, showing no degradation compared to the baseline models.
- Lastly, as we explicitly render each scene in our NeRF dataset from various viewpoints, simulating real camera motion instead of relying on homography to mimic camera motions, we explore whether models supervised by the PrP process during training demonstrate improvement in their relative pose estimation capabilities.

5.1 Homography Estimation

Following [23, 6, 22, 14, 7] we evaluate homography estimation on the HPatches dataset [39]. The HPatches dataset consist of 57 scenes with varying illumination, and 59 scenes with large viewpoint variation. Each scene contains 6 images, related by ground truth homographies.

Table 1: **HPatches Metrics.** Both baseline SiLK [14] and SuperPoint [6], surpass SiLK-PrP and SuperPoint-PrP on HPatches metrics.

	Rep. \uparrow		Hom. Est. Acc. \uparrow		Hom. Est. AUC \uparrow		MMA \uparrow		MS \uparrow
	$\epsilon = 3$	$\epsilon = 5$	$\epsilon = 3$	$\epsilon = 5$	$\epsilon = 3$	$\epsilon = 5$	$\epsilon = 3$	$\epsilon = 5$	
SP	0.60	0.70	0.80	0.86	0.53	0.65	0.61	0.65	0.46
SP-PrP-Hyb	0.56	0.66	0.76	0.85	0.50	0.62	0.60	0.66	0.45
SP-PrP	0.54	0.67	0.73	0.82	0.47	0.60	0.58	0.66	0.42
SiLK	0.77	0.85	0.84	0.90	0.65	0.74	0.66	0.67	0.38
SiLK-PrP	0.72	0.80	0.75	0.81	0.54	0.64	0.62	0.63	0.31
SiLK-PrP-Aug	0.74	0.82	0.78	0.85	0.56	0.67	0.60	0.61	0.32

Table 2: **HPatches metrics separated.** SiLK-PrP and SiLK are similar in estimating homography for scenes with varying viewpoints, while SiLK-PrP falls behind in varying illumination scenes.

	HPatches Viewpoint				HPatches Illumination			
	Rep. \uparrow		Hom. Est. Acc. \uparrow		Rep. \uparrow		Hom. Est. Acc. \uparrow	
	$\epsilon = 3$	$\epsilon = 5$	$\epsilon = 3$	$\epsilon = 5$	$\epsilon = 3$	$\epsilon = 5$	$\epsilon = 3$	$\epsilon = 5$
SiLK	0.79	0.86	0.73	0.84	0.75	0.84	0.95	0.96
SiLK-PrP-Aug	0.79	0.87	0.71	0.81	0.69	0.77	0.87	0.89

5.1.1 Evaluation Protocol.

We follow [23, 14] are resize the shorter image side to a dimension of 480. To evaluate interest point detection quality and performance, we report the repeatability metric as in [6, 14]. Moreover, we evaluate the keypoint descriptors, we report the mean matching accuracy (MMA) *i.e.* the ratio of matches where reprojection error is below a specified threshold [20]; and matching score *i.e.* The ratio between correctly matched points and total number of detected points. Lastly, we use OpenCV with RANSAC algorithm to estimate the homography between an image pair, and report the homography estimation accuracy and area under the curve (AUC) error over all image pairs. We keep the top 1k detected interest points for SuperPoint and 10k for SiLK.

5.1.2 Baselines.

We assess SuperPoint-PrP by comparing it to the baseline SuperPoint model [6]. Additionally, we introduce a hybrid variant of SuperPoint-PrP denoted as "SP-PrP-Hyb". This variant incorporates the MagicPoint model, trained through two rounds of Homographic Adaptation, followed by training SuperPoint model on the NeRF dataset using our PrP process and Projective Adaptation. Furthermore, we present two versions of PrP SiLK models; the first, SiLK-PrP, is trained without rotation or scaling augmentation as detailed in Sec. 4.1. The second, SiLK-PrP-Aug, includes rotation and scaling during training.

5.1.3 Results.

As seen in Tab. 1, the PrP trained models are outperformed by their baseline counterparts [14, 6] in all of the HPatches metrics. Nonetheless, this outcome is expected as both SiLK-PrP and SuperPoint-PrP are not rotation or scale invariant, in contrast to their corresponding baseline models. On the other hand, despite SiLK-PrP-Aug's efforts to incorporate in-place augmentation for rotation and scale invariance (see Fig. 4), it falls short compared to the SiLK model.

Tab. 2 further delves into SiLK-PrP-Aug's homography estimation performance, revealing its homography estimation aligns with SiLK in scenes with varying viewpoints. However, a dip in performance is observed in scenes with varying illumination conditions. This discrepancy contributes to the observed performance gap between SiLK-PrP-Aug and SiLK [14] in Tab. 1. We opted to use the same photometric augmentation used for SiLK [14] when training SiLK-PrP and SiLK-PrP-Aug, however, optimising photometric augmentation parameters during training SiLK-PrP and SiLK-PrP-Aug on the NeRF dataset might offer improved results.

5.2 Relative Pose Estimation

For evaluating the relative pose estimation on indoor scenes, we leverage the ScanNet dataset [18]. We employ the 1500 test image pairs provided by [22].

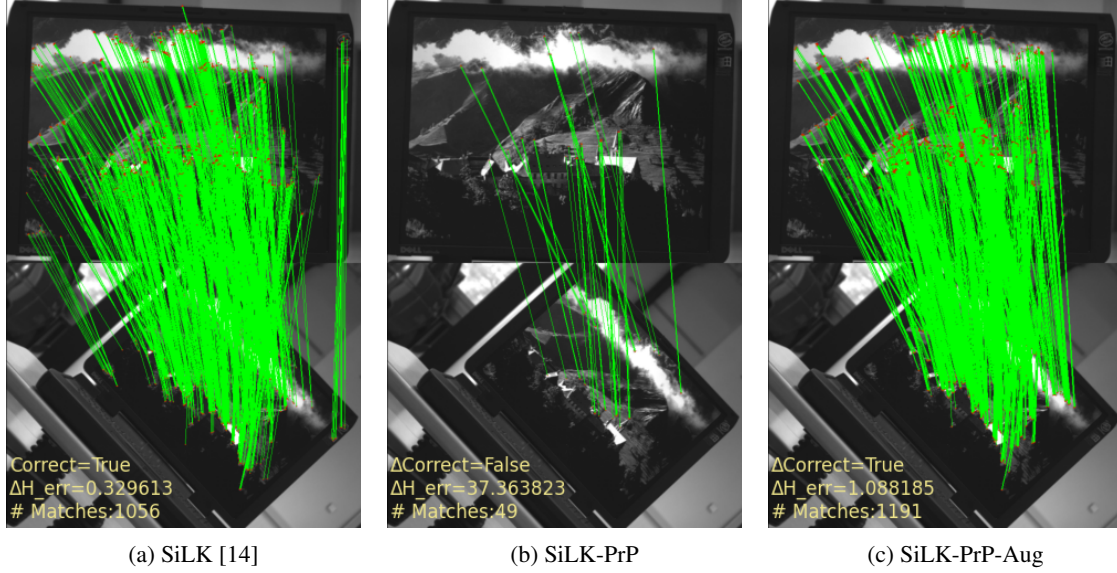


Figure 4: **Rotation and Scale invariance.** In Fig. 4b, it is evident that SiLK-PrP lacks rotation and scale invariance compared to SiLK (see Fig. 4a) [14]. Incorporating rotation and scaling SiLK-PrP’s training process, rotation and scale invariance is achieved (see Fig. 4c).

To assess pose estimation on outdoor scenes, we employ the YFCC100M dataset [40]. We utilise the YFCC100M test split introduced by [22]. This split samples 1000 image pairs from four scenes each, thus, the total number of image pairs for the outdoor pose evaluation is 4000 image pairs.

5.2.1 Evaluation Protocol.

For indoor relative pose evaluation, we follow [23, 22] and resize ScanNet’s images to a size of $[640 \times 480]$. For SuperPoint, we use the top 1k predicted points and 20k for SiLK.

Additionally, for outdoor relative pose evaluation, we resize the YFCC100M images so that the longest dimension is equal to 1200. We use the top 2k predicted points for SuperPoint and 20k for SiLK.

For both indoor and outdoor pose evaluations, we report the pose error AUC at thresholds (5° , 10° , 20°), where the pose error is the maximum between the angular rotation error and angular translation error. Furthermore, we compute the essential matrix using the matched interest points using OpenCV with a RANSAC threshold of 0.5 over the mean of the focal length.

5.2.2 Baselines.

Similar to the Homography Estimation evaluation Sec. 5.1, we compare SuperPoint-PrP and SuperPoint-PrP-Hyb with the baseline SuperPoint model. Likewise, we assess SiLK-PrP and SiLK-PrP-Aug against the baseline SiLK model.

5.2.3 Indoor Pose Estimation Results.

As depicted in Tab. 3, the PrP models consistently surpass their respective baseline counterparts across all angular pose error thresholds. Although performance enhancement for SuperPoint-PrP and SuperPoint-PrP-Hyb over SuperPoint [6] is marginal, a more substantial improvement is evident in the case of SiLK-PrP and SiLK-PrP-Aug in comparison to SiLK [14], particularly as the angular threshold increases.

Unfortunately, the relative pose estimation computes the translation error as the angular translation error between the ground truth and estimated translation vectors. The computed angular translation error suffers from instability as it could only be computed up to a certain scale factor [42, 43]. This instability could be seen in Fig. 5, where it is evident that the angular translation error is unstable when the norm of the ground truth relative translation vector ($\|t_{GT}\|$) is approximately 0.2 and below.

To address this issue, we refined the indoor relative pose estimation assessment. For scenes where $\|t_{GT}\|$ is below the threshold ϵ set at 0.15, we exclusively report the pose error AUC based on angular rotation error. Furthermore,

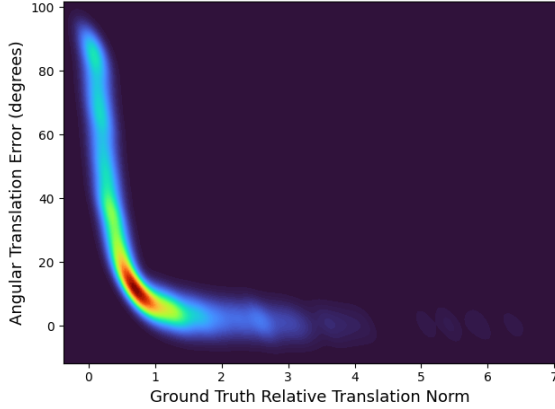


Figure 5: **Instability in Angular Translation Error.** Density plot illustrating how the angular translation error is unstable in situations where the ground truth relative translation between two camera viewpoints is minimal.

Table 3: **Indoor Relative Pose Estimation Error AUC.** The models trained using the PrP process outperform their respective baseline models [14, 6] in accurately estimating relative poses within indoor scenes for all reported angular thresholds.

Pose Est. AUC	@5° ↑	@10° ↑	@20° ↑
SP	4.95	11.90	21.67
SP-PrP-Hyb	<u>5.78</u>	<u>13.52</u>	<u>24.74</u>
SP-PrP	5.20	12.53	22.82
SiLK	7.18	16.14	27.84
SiLK-PrP	9.42	20.17	32.31
SiLK-PrP-Aug	<u>9.60</u>	<u>20.75</u>	<u>34.24</u>

Table 4: **Separated Indoor Relative Pose Estimation Error AUC.** For image pairs with minimal relative translation in viewpoints, the PrP models exhibit superior performance in accurately estimating the relative rotation, especially the SuperPoint-PrP and SiLK-PrP-Aug models.

Pose Est. AUC	Pose Est. AUC $\ t_{gt}\ \leq \epsilon$ Rot., 157 image pairs			Pose Est. AUC $\ t_{gt}\ > \epsilon$ max (Rot., Transl.), 1363 image pairs		
	@5° ↑	@10° ↑	@20° ↑	@5° ↑	@10° ↑	@20° ↑
SP	50.34	60.87	82.58	5.21	12.19	22.19
SP-PrP-Hyb	47.56	67.95	81.27	<u>6.14</u>	<u>14.22</u>	<u>25.45</u>
SP-PrP	<u>51.21</u>	<u>69.67</u>	<u>82.36</u>	5.42	12.94	23.14
SiLK	54.33	73.02	85.24	7.62	17.02	28.82
SiLK-PrP	57.59	74.19	85.28	<u>10.22</u>	21.53	33.52
SiLK-PrP-Aug	<u>57.60</u>	<u>75.54</u>	<u>86.38</u>	<u>10.22</u>	<u>21.79</u>	<u>35.07</u>

for scenes where the threshold ϵ exceeds 0.15, we report the pose error AUC as the maximum value between angular rotation error and angular translation error. As presented in Tab. 4, it is evident that all models excel in estimating relative rotation in scenes characterised by minimal translation between viewpoints. Notably, the PrP models exhibit a slight performance advantage over their baseline counterparts in this specific scenario. Additionally, in scenes where the ground truth relative translation exceeds the defined threshold, further improvement can be observed for the PrP models compared to results reported in Tab. 3.

5.2.4 Outdoor Pose Estimation Results.

Similar to results obtained in Tab. 3, the PrP models surpass their corresponding baseline models in relative pose estimation for outdoor scenes, as observed by results shown in Tab. 5. The results reported in Tabs. 3 to 5 collectively highlight that models subjected to PrP supervision during training demonstrate significant improvement in their relative pose estimation capability.

5.3 Pairwise Point Cloud Registration

We follow recent work [44, 14] and evaluate the interest point detectors and descriptors on a 3D point cloud registration task. Evaluation is performed on ScanNet’s [18] official test split, where image pairs are sampled 20 frames apart.

5.3.1 Evaluation Protocol.

The point cloud registration evaluation is conducted by resizing the ScanNet [18] images to dimensions of $[128 \times 128]$. Given a pair of RGB-D images, a 6-DOF pose is estimated that best aligns the first image to the second image. The

Table 5: **Outdoor Relative Pose Estimation Error AUC.** The PrP trained models exhibit superior performance compared to their baseline counterparts [14, 6] in estimating relative poses for outdoor scenes, similar to observed results in Tab. 3

Pose Est. AUC	@5° ↑	@10° ↑	@20° ↑
SP	6.97	14.89	25.96
SP-PrP-Hyb	<u>9.58</u>	<u>19.62</u>	<u>32.32</u>
SP-PrP	9.02	18.27	30.33
SiLK	7.82	15.05	24.93
SiLK-PrP	<u>9.44</u>	<u>17.31</u>	<u>27.04</u>
SiLK-PrP-Aug	7.82	14.33	22.52

Table 6: **Point Cloud Reg.** SuperPoint-PrP and SuperPoint-PrP demonstrate marginal enhancements over the baseline SuperPoint model. Meanwhile, SiLK-PrP and SiLK-PrP-Aug maintain competitiveness with the baseline SiLK model.

	Rot.					Transl.					Chamfer				
	Acc. ↑			Err. ↓		Acc. ↑			Err. ↓		Acc. ↑			Err. ↓	
	5°	10°	45°	M.	Med.	5	10	25	M.	Med.	1	5	10	M.	Med.
SP	79.8	90.3	98.1	5.7	2.2	45.4	70.6	89.0	13.5	5.6	62.9	84.4	89.5	9.4	0.5
SP-PrP-Hyb	<u>82.0</u>	<u>92.0</u>	<u>98.5</u>	<u>5.2</u>	<u>2.2</u>	44.0	<u>72.5</u>	<u>91.6</u>	<u>12.0</u>	5.7	<u>64.4</u>	<u>87.1</u>	<u>91.9</u>	<u>7.0</u>	<u>0.5</u>
SP-PrP	81.4	91.9	98.4	<u>5.2</u>	2.3	43.3	71.6	91.5	12.1	5.8	63.9	<u>87.1</u>	<u>91.9</u>	7.9	<u>0.5</u>
SiLK	<u>95.6</u>	<u>97.5</u>	<u>99.1</u>	<u>2.6</u>	0.8	<u>79.9</u>	<u>91.4</u>	<u>96.9</u>	<u>6.1</u>	2.2	<u>89.4</u>	<u>95.8</u>	<u>97.1</u>	<u>4.7</u>	<u>0.1</u>
SiLK-PrP	93.0	96.2	98.7	3.4	1.0	71.3	87.0	95.3	8.1	2.8	84.3	93.7	95.7	5.7	<u>0.1</u>
SiLK-PrP-A.	94.6	97.2	99.0	2.8	0.9	75.0	89.5	96.4	7.0	2.5	86.8	95.1	96.7	5.4	<u>0.1</u>

metrics reported during evaluation are angular rotation and translation errors in degrees and centimetres respectively. Moreover, the chamfer distance is also reported between the ground-truth point cloud and the reconstructed point cloud in centimetres. For all three reported metrics the accuracy, mean and median errors over the entire dataset are reported at different thresholds [44].

5.3.2 Baselines.

Unlike previous evaluations (Secs. 5.1 and 5.2) where sparse feature matching was employed, we follow [44, 14] and perform the point cloud registration using dense feature matching. The ratio-test is utilised to find correspondences and alignment is seen as Procrustes problem solved by a weighted Kabsch’s algorithm. [45, 46, 14].

5.3.3 Results.

As depicted in Tab. 6, both SuperPoint-PrP and SuperPoint-PrP-Hyb consistently outperform the baseline SuperPoint model across all metrics by a small margin, except for translation at a 5 cm threshold. Moreover, SiLK generally maintains a 1-3% advantage over SiLK-PrP and SiLK-PrP-Aug, except at a 5 cm translation threshold, where it stands at 5%; however, the SiLK PrP trained models remain competitive with the baseline SiLK model.

It is essential to highlight that SiLK is trained on a relatively small image size of [164x164], whereas the NeRF dataset comprises larger images [640x480]. Since the point cloud registration is conducted on an image size of [128x128], it is expected that SiLK outperforms SiLK-PrP at lower image dimensions, however, results also indicate that the SiLK PrP trained models could detect high quality interest points at low resolutions.

6 Conclusion

This paper introduces a novel approach to supervise learning-based feature point detectors and descriptors, leveraging perspective projective geometry on synthesised NeRF data. Despite the fact that our proposed dataset is exclusively composed of synthetic images rather than real RGB images, and is comparatively smaller than large open-source datasets, results indicated there was no observed decrease in generalisability or feature point detection quality. As expected our models generally outperform homography-trained baselines on multi-view benchmarks with highly non-planar scenes, while slightly underperforming on a homography estimation benchmark. The larger potential for further advancements lies in improving the quality of training data with advances in neural rendering that can generate higher quality synthesised images devoid of artefacts, and most importantly more precise depth maps to avoid misprojection errors.

References

- [1] Onur Ozyesil, Vladislav Voroninski, Ronen Basri, and Amit Singer. A survey of structure from motion, 2017.
- [2] Takafumi Taketomi, Hideaki Uchiyama, and Sei Ikeda. Visual slam algorithms: a survey from 2010 to 2016. *IPSN Transactions on Computer Vision and Applications*, 9(1):16, Jun 2017.
- [3] Iman Abaspor Kazerouni, Luke Fitzgerald, Gerard Dooly, and Daniel Toal. A survey of state-of-the-art on visual slam. *Expert Systems with Applications*, 205:117734, 2022.
- [4] Stephanie Lowry, Niko Sünderhauf, Paul Newman, John J. Leonard, David Cox, Peter Corke, and Michael J. Milford. Visual place recognition: A survey. *IEEE Transactions on Robotics*, 32(1):1–19, 2016.
- [5] Xiwu Zhang, Lei Wang, and Yan Su. Visual place recognition: A survey from deep learning perspective. *Pattern Recognition*, 113:107760, 2021.
- [6] Daniel DeTone, Tomasz Malisiewicz, and Andrew Rabinovich. Superpoint: Self-supervised interest point detection and description. *CoRR*, abs/1712.07629, 2017.
- [7] Jerome Revaud, Philippe Weinzaepfel, César De Souza, Noe Pion, Gabriela Csurka, Yohann Cabon, and Martin Humenberger. R2d2: Repeatable and reliable detector and descriptor. *arXiv preprint arXiv:1906.06195*, 2019.
- [8] Xiaoming Zhao, Xingming Wu, Jinyu Miao, Weihai Chen, Peter C. Y. Chen, and Zhengguo Li. Alike: Accurate and lightweight keypoint detection and descriptor extraction. *IEEE Transactions on Multimedia*, 25:3101–3112, 2023.
- [9] Jiexiong Tang, Ludvig Ericson, John Folkesson, and Patric Jensfelt. Gcnv2: Efficient correspondence prediction for real-time slam. *IEEE Robotics and Automation Letters*, 4(4):3505–3512, 2019.
- [10] Guangqiang Li, Lei Yu, and Shumin Fei. A deep-learning real-time visual slam system based on multi-task feature extraction network and self-supervised feature points. *Measurement*, 168:108403, 2021.
- [11] Hudson Martins Silva Bruno and Esther Luna Colombini. Lift-slam: A deep-learning feature-based monocular visual slam method. *Neurocomputing*, 455:97–110, September 2021.
- [12] Aji Resindra Widya, Akihiko Torii, and Masatoshi Okutomi. Structure-from-motion using dense cnn features with keypoint relocalization, 2018.
- [13] Matthew Tancik, Ethan Weber, Evonne Ng, Ruilong Li, Brent Yi, Terrance Wang, Alexander Kristoffersen, Jake Austin, Kamyar Salahi, Abhik Ahuja, David Mcallister, Justin Kerr, and Angjoo Kanazawa. Nerfstudio: A modular framework for neural radiance field development. In *ACM SIGGRAPH 2023 Conference Proceedings*, SIGGRAPH ’23, New York, NY, USA, 2023. Association for Computing Machinery.
- [14] Pierre Gleize, Weiyao Wang, and Matt Feiszli. Silk: Simple learned keypoints. In *Proceedings of the IEEE/CVF International Conference on Computer Vision (ICCV)*, pages 22499–22508, October 2023.
- [15] David G. Lowe. Distinctive Image Features from Scale-Invariant Keypoints. *International Journal of Computer Vision*, 60(2):91–110, November 2004.
- [16] Ethan Rublee, Vincent Rabaud, Kurt Konolige, and Gary Bradski. Orb: An efficient alternative to sift or surf. In *2011 International Conference on Computer Vision*, pages 2564–2571, 2011.
- [17] Tsung-Yi Lin, Michael Maire, Serge Belongie, James Hays, Pietro Perona, Deva Ramanan, Piotr Dollár, and C. Lawrence Zitnick. Microsoft coco: Common objects in context. In David Fleet, Tomas Pajdla, Bernt Schiele, and Tinne Tuytelaars, editors, *Computer Vision – ECCV 2014*, pages 740–755, Cham, 2014. Springer International Publishing.
- [18] Angela Dai, Angel X. Chang, Manolis Savva, Maciej Halber, Thomas A. Funkhouser, and Matthias Nießner. Scannet: Richly-annotated 3d reconstructions of indoor scenes. *CoRR*, abs/1702.04405, 2017.
- [19] Zhengqi Li and Noah Snavely. Megadepth: Learning single-view depth prediction from internet photos. In *2018 IEEE/CVF Conference on Computer Vision and Pattern Recognition*, pages 2041–2050, 2018.
- [20] Michal J. Tyszkiewicz, Pascal Fua, and Eduard Trulls. DISK: learning local features with policy gradient. *CoRR*, abs/2006.13566, 2020.
- [21] Mihai Dusmanu, Ignacio Rocco, Tomas Pajdla, Marc Pollefeys, Josef Sivic, Akihiko Torii, and Torsten Sattler. D2-net: A trainable cnn for joint description and detection of local features. In *2019 IEEE/CVF Conference on Computer Vision and Pattern Recognition (CVPR)*, pages 8084–8093, 2019.
- [22] Paul-Edouard Sarlin, Daniel DeTone, Tomasz Malisiewicz, and Andrew Rabinovich. Superglue: Learning feature matching with graph neural networks. In *2020 IEEE/CVF Conference on Computer Vision and Pattern Recognition (CVPR)*, pages 4937–4946, 2020.

- [23] Jiaming Sun, Zehong Shen, Yuang Wang, Hujun Bao, and Xiaowei Zhou. Loftr: Detector-free local feature matching with transformers. In *2021 IEEE/CVF Conference on Computer Vision and Pattern Recognition (CVPR)*, pages 8918–8927, 2021.
- [24] Wei Jiang, Eduard Trulls, Jan Hosang, Andrea Tagliasacchi, and Kwang Moo Yi. Cotr: Correspondence transformer for matching across images. In *2021 IEEE/CVF International Conference on Computer Vision (ICCV)*, pages 6187–6197, 2021.
- [25] Thomas Müller, Alex Evans, Christoph Schied, and Alexander Keller. Instant neural graphics primitives with a multiresolution hash encoding. *ACM Trans. Graph.*, 41(4):102:1–102:15, July 2022.
- [26] Jonathan T. Barron, Ben Mildenhall, Matthew Tancik, Peter Hedman, Ricardo Martin-Brualla, and Pratul P. Srinivasan. Mip-nerf: A multiscale representation for anti-aliasing neural radiance fields. *CoRR*, abs/2103.13415, 2021.
- [27] J. T. Barron, B. Mildenhall, D. Verbin, P. P. Srinivasan, and P. Hedman. Zip-nerf: Anti-aliased grid-based neural radiance fields. In *2023 IEEE/CVF International Conference on Computer Vision (ICCV)*, pages 19640–19648, Los Alamitos, CA, USA, oct 2023. IEEE Computer Society.
- [28] Casimir Feldmann, Niall Siegenheim, Nikolas Hars, Lovro Rabuzin, Mert Ertugrul, Luca Wolfart, Marc Pollefeys, Zuria Bauer, and Martin R. Oswald. Nerfmentation: Nerf-based augmentation for monocular depth estimation, 2024.
- [29] Lin Yen-Chen, Pete Florence, Jonathan T. Barron, Tsung-Yi Lin, Alberto Rodriguez, and Phillip Isola. Nerf-supervision: Learning dense object descriptors from neural radiance fields. In *2022 International Conference on Robotics and Automation (ICRA)*, page 6496–6503. IEEE Press, 2022.
- [30] F. Tosi, A. Tonioni, D. De Gregorio, and M. Poggi. Nerf-supervised deep stereo. In *2023 IEEE/CVF Conference on Computer Vision and Pattern Recognition (CVPR)*, pages 855–866, Los Alamitos, CA, USA, jun 2023. IEEE Computer Society.
- [31] Han Ling. Adfactory: An effective framework for generalizing optical flow with nerf, 2023.
- [32] Benedikt Bitterli. Rendering resources, 2016. <https://benedikt-bitterli.me/resources/>.
- [33] Jonathan T. Barron, Ben Mildenhall, Dor Verbin, Pratul P. Srinivasan, and Peter Hedman. Mip-nerf 360: Unbounded anti-aliased neural radiance fields. In *2022 IEEE/CVF Conference on Computer Vision and Pattern Recognition (CVPR)*, pages 5460–5469, 2022.
- [34] Johannes L. Schonberger and Jan-Michael Frahm. Structure-from-motion revisited. In *Proceedings of the IEEE Conference on Computer Vision and Pattern Recognition (CVPR)*, June 2016.
- [35] Ricardo Martin-Brualla, Noha Radwan, Mehdi S. M. Sajjadi, Jonathan T. Barron, Alexey Dosovitskiy, and Daniel Duckworth. Nerf in the wild: Neural radiance fields for unconstrained photo collections. In *2021 IEEE/CVF Conference on Computer Vision and Pattern Recognition (CVPR)*, pages 7206–7215, 2021.
- [36] Thomas Müller, Alex Evans, Christoph Schied, and Alexander Keller. Instant neural graphics primitives with a multiresolution hash encoding. *ACM Trans. Graph.*, 41(4):102:1–102:15, July 2022.
- [37] Zirui Wang, Shangzhe Wu, Weidi Xie, Min Chen, and Victor Adrian Prisacariu. NeRF—: Neural radiance fields without known camera parameters. *arXiv preprint arXiv:2102.07064*, 2021.
- [38] Adam Paszke, Sam Gross, Francisco Massa, Adam Lerer, James Bradbury, Gregory Chanan, Trevor Killeen, Zeming Lin, Natalia Gimelshein, Luca Antiga, Alban Desmaison, Andreas Köpf, Edward Z. Yang, Zach DeVito, Martin Raison, Alykhan Tejani, Sasank Chilamkurthy, Benoit Steiner, Lu Fang, Junjie Bai, and Soumith Chintala. Pytorch: An imperative style, high-performance deep learning library. *CoRR*, abs/1912.01703, 2019.
- [39] Vassileios Balntas, Karel Lenc, Andrea Vedaldi, and Krystian Mikolajczyk. Hpatches: A benchmark and evaluation of handcrafted and learned local descriptors. In *CVPR*, 2017.
- [40] Bart Thomee, David A. Shamma, Gerald Friedland, Benjamin Elizalde, Karl Ni, Douglas Poland, Damian Borth, and Li-Jia Li. The new data and new challenges in multimedia research. *CoRR*, abs/1503.01817, 2015.
- [41] Torsten Sattler, Will Maddern, Carl Toft, Akihiko Torii, Lars Hammarstrand, Erik Stenborg, Daniel Safari, Masatoshi Okutomi, Marc Pollefeys, Josef Sivic, Fredrik Kahl, and Tomas Pajdla. Benchmarking 6dof outdoor visual localization in changing conditions. In *2018 IEEE/CVF Conference on Computer Vision and Pattern Recognition*, pages 8601–8610, 2018.
- [42] R. I. Hartley and A. Zisserman. *Multiple View Geometry in Computer Vision*. Cambridge University Press, ISBN: 0521540518, second edition, 2004.

- [43] Kwang Moo Yi, Eduard Trulls, Yuki Ono, Vincent Lepetit, Mathieu Salzmann, and Pascal Fua. Learning to find good correspondences. In *2018 IEEE/CVF Conference on Computer Vision and Pattern Recognition*, pages 2666–2674, 2018.
- [44] Mohamed El Banani, Luya Gao, and Justin Johnson. UnsupervisedR&R: Unsupervised Point Cloud Registration via Differentiable Rendering. In *CVPR*, 2021.
- [45] W. Kabsch. A solution for the best rotation to relate two sets of vectors. *Acta Crystallographica Section A*, 32(5):922–923, Sep 1976.
- [46] Christopher Choy, Wei Dong, and Vladlen Koltun. Deep global registration. In *2020 IEEE/CVF Conference on Computer Vision and Pattern Recognition (CVPR)*, pages 2511–2520, 2020.